Spin-polarized white organic light-emitting diodes based on chirality-induced spin selectivity effect

Letian Xu,[1] Nuoling Qiu,[1] Xiaoluo Peng,[1] Kun Zhou,[2] Jiajie Zeng,[1] Hao Liu,[1] Ben Zhong Tang[2] and Zujin Zhao*[,1]

[1] State Key Laboratory of Luminescent Materials and Devices, Guangdong Provincial Key Laboratory of Luminescence from Molecular Aggregates, South China University of Technology, 510640 Guangzhou, China. E-mail: mszjzhao@scut.edu.cn

[2] School of Science and Engineering, The Chinese University of Hong Kong, Shenzhen (CUHK-Shenzhen), Guangdong, 518172, China

Abstract

Chirality-induced spin selectivity (CISS) effect refers to charge carriers become spin-polarized when traversing through chiral materials, but this unique phenomenon has never been reported for organic light-emitting diodes (OLEDs). Herein, robust chiral near-ultraviolet and deep-blue materials with wide energy gaps are explored and demonstrated to possess CISS effect. By aligning a chiral deep-blue layer next to an achiral green layer in OLEDs, spin-polarized charge carriers are generated from the chiral layer and get recombined to form spin-polarized excitons in the adjacent achiral green layer, furnishing green circularly polarized electroluminescence (CP-EL). Furthermore, by incorporating multiple achiral sky-blue, green and red layers with chiral near-ultraviolet or deep-blue layers, complex three-emitting-layer or four-emitting-layer spin-polarized white OLEDs are realized, providing distinct CP-EL signals from different achiral emitting layers simultaneously and outstanding EL performance with excellent external quantum efficiencies reaching 26.6% and high color rendering indexes of 94, much superior to the performances of the reported white OLEDs with circularly polarized light so far. This work introduces CISS effect into OLEDs for achieving CP-EL for the first time, and virtually presents a novel and feasible approach towards high-performance circularly polarized white OLEDs with a single organic chiral layer.

Introduction

Circularly polarized organic light-emitting diodes (OLEDs) own the capability to directly radiate left- or right-hand circularly polarized electroluminescence (CP-EL), and have attracted increasing attention in 3D display and quantum computing, among other applications[1-5]. These OLEDs can be made into flexible, ultrathin and transparent patterns, becoming a promising technique for high-tech devices[6-9]. The conventional approach for fabricating circularly polarized OLEDs mainly focuses on the design and synthesis of efficient organic materials with circularly polarized luminescence, which are subsequently utilized as the emitting centers in light-emitting layers (EMLs)[10-12]. Alternatively, circularly polarized OLEDs can also be obtained based on chirality-induction strategy of blending a chirality inducer with emitting materials during the preparation of the EMLs[13-15]. Essentially, the chiral nature of these devices originates from the chiral emitting materials or the chiral environments in EMLs[16-18]. In general, once multiple emission colors are required, such as in circularly polarized white OLEDs, various efficient chiral emitting materials and well-matched chiral hosts are needed, which sets high and complicated requirements for both chiral emitters and hosts[19-24].

Chirality-induced spin selectivity (CISS) effect is a unique phenomenon that charge carriers become spin-polarized when traversing through chiral materials, which provides modulation possibility between the spin of charge carriers and chirality[25-31]. Compared with the traditional methods that always require ferromagnetic contact, low temperature or external magnetic field, the CISS effect could be a more facile and effective approach to control the spin of charge carriers[32-44]. Based on CISS effect, CP-EL can be realized in spin-polarized light-emitting diodes (spin-LEDs), in which spin-polarized electrons (or holes) are recombined with unpolarized holes (or electrons) to form spin-polarized carrier pairs, namely spin-polarized excitons[45,46]. However, the reported CISS effect driven room

https://doi.org/10.26434/chemrxiv-2024-qw671 ORCID: https://orcid.org/0000-0002-0618-6024 Content not peer-reviewed by ChemRxiv. License: CC BY 4.0

temperature spin-LEDs rely on the chiral metal-halide perovskite hybrid semiconductor to generate spin-polarized charge carriers, which make the color modulation of CP-EL difficult[47-49], let alone achieving white CP-EL in a single spin-LED device. Recently, some organic chiral materials are demonstrated to have CISS effect at room temperature[50-52], which inspires us to harness CISS effect to acquire spin-polarized charge carriers for the construction of spin-polarized OLEDs (spin-OLEDs) with organic chiral materials. Given that the emission properties of organic materials can be precisely regulated in a wide region, it is envisioned that multilayer spin-OLEDs with diverse CP-EL colors and even white light can be achieved by ingenious designs of organic chiral materials as well as rational engineering of device configurations[53,54].

In this work, we wish to report a universal methodology for the fabrication of spin-OLEDs based on CISS effect, and highly efficient green and white spin-OLEDs are successfully prepared, providing prominent green and white CP-EL signals with outstanding EL efficiencies. Initially, chiral near-ultraviolet and deep-blue materials with wide energy gaps are explored and demonstrated to possess CISS effect. In consequence, spin-polarized charge carriers are generated from these achiral layers and get recombined to form spin-polarized excitons in adjacent achiral green layers, furnishing spin-OLEDs with green CP-EL. Unlike the current chirality-induction method for obtaining CP-EL, which involves doping achiral emitter into chiral host (or vice versa) in the same one layer, in these new spin-OLEDs, the chirality-induction effect is eliminated by separating the chiral layer and the achiral layer into two different layers. Furthermore, by incorporating multiple achiral sky-blue, green and red layers with chiral near-ultraviolet or deep-blue layers, complex three-emitting-layer or four-emitting-layer spin-polarized white OLEDs (spin-WOLEDs) are obtained (Fig. 1a), providing distinct CP-EL signals from different achiral emitting layers and outstanding EL performance with a best external quantum efficiency of 26.6% and a highest CRI of 94 reported for circularly polarized WOLEDs to date.

Results

Materials and Characterization

The chiral and achiral materials used in the following experiments are shown in Fig. 1b. The achiral green (BDMAC-XT) emitters with thermally activated delayed fluorescence (TADF) property are prepared according to the reported methods[55], and the achiral sky-blue TADF emitter (DMAC-DPS) and red emitter (DBP) with normal fluorescence characteristic is acquired from commercial source. The new chiral near-ultraviolet ((*S*)-/(*R*)-PCNCP) and deep-blue ((*S*)-/(*R*)-PCNTPA) materials are synthesized facilely following the synthetic routes in Supplementary Scheme 1, and

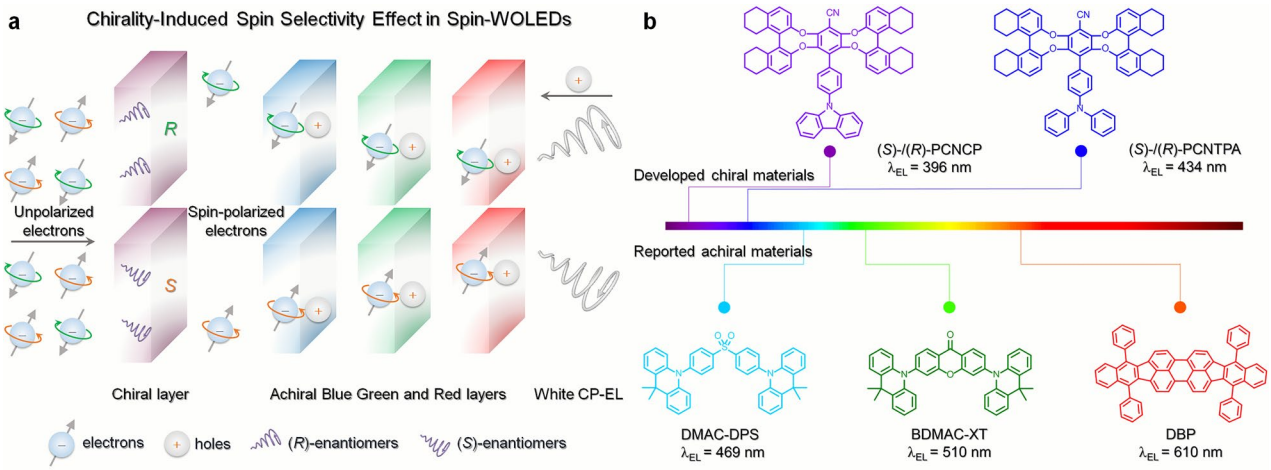

Fig. 1 | Design concept of spin-WOLEDs based on CISS effect. **a**, Illustration of spin-polarized charge carriers and spin-polarized excitons in spin-WOLEDs. **b**, Molecular structures of chiral near-ultraviolet ((*S*)-/(*R*)-PCNCP) and deep-blue ((*S*)-/(*R*)-PCNTPA) materials, and achiral sky-blue (DMAC-DPS), green (BDMAC-XT) and red (DBP) materials.

https://doi.org/10.26434/chemrxiv-2024-qw671 ORCID: https://orcid.org/0000-0002-0618-6024 Content not peer-reviewed by ChemRxiv. License: CC BY 4.0

their structures are confirmed using NMR and high-resolution mass spectrometry.

Concerning the nearly identical properties of the (*S*)-/(*R*)-enantiomers, (*S*)-PCNCP and (*S*)-PCNTPA are selected as representative examples for property investigation. (*S*)-PCNCP and (*S*)-PCNTPA exhibit high decomposition temperatures of 468 and 483 °C, respectively, indicative of robust thermal stability. A high glass-transition temperature of 180 °C is observed for (*S*)-PCNTPA, implying its good morphological stability (Supplementary Fig. 1). Moreover, they display reversible oxidation processes in cyclic voltammetry experiment (Supplementary Fig. 2). The energy levels of the highest occupied molecular orbitals (HOMOs) are calculated as –5.63 and –5.28 eV for (*S*)-PCNCP and (*S*)-PCNTPA, respectively, from the onset potentials of oxidation waves. The optical energy gaps are calculated as 3.52 and 3.17 eV for (*S*)-PCNCP and (*S*)-PCNTPA, respectively, from the onsets of UV-vis absorption spectra. In consequence, the energy levels of the lowest unoccupied molecular orbitals (LUMOs) are calculated as –2.11 and –2.11 eV for (*S*)-PCNCP and (*S*)-PCNTPA, respectively.

Theoretical calculations reveal that the HOMOs and LUMOs of these chiral materials are primarily localized on the donors of carbazole, triphenylamine, and the acceptor of benzonitrile, respectively, but have partial overlap on the phenyl bridge (Supplementary Fig. 3). The inadequate separation between HOMOs and LUMOs results in substantial theoretical energy gaps of 0.95 and 0.83 eV for (*S*)-PCNCP and (*S*)-PCNTPA between the lowest excited triplet (T_1) and singlet (S_1) states, suggesting that the reverse intersystem crossing (RISC) process from T_1 to S_1 states is unlikely to occur in these materials. However, there are small energy gaps (0.08–0.22 eV) between high-lying excited triplet (T_2–T_4) states and S_1 state, whereas the energy gaps between T_2 and T_1 states are as large as 0.87 and 0.98 eV, respectively. Additionally, considerable spin-orbital coupling (SOC) matrix elements are found between T_2–T_4 and S_1 states. For example, the SOC matrix elements between T_2 and S_1 states are 1.108 and 0.760 cm^{-1} for (*S*)-PCNCP and (*S*)-PCNTPA, respectively (Supplementary Fig. 3). These simulation results suggest that the high-lying RISC (hRISC) process may occur in these chiral materials, which is conducive to increasing exciton utilization and improving EL efficiencies.

Photophysical and chiral property

(*S*)-PCNCP and (*S*)-PCNTPA in dilute toluene solutions exhibit absorption maxima at 310 and 320 nm and photoluminescence (PL) peaks at 390 and 423 nm, respectively. In neat films, (*S*)-PCNCP and (*S*)-PCNTPA display robust PL emissions peaking at 404 and 439 nm, with high PL quantum yields (Φ_{PL}s) of 91% and 85%, respectively. The doped films of 25 wt% (*S*)- PCNCP and 40 wt% (*S*)-PCNTPA in 2,6-bis(carbazol-9-yl)pyridine (PYD-2) host show nearly unchanged PL spectra, and excellent Φ_{PL}s of 97% and 95%, respectively (Fig. 2a and 2b, and Supplementary Table 1). The transient PL decay spectra of (*S*)-PCNCP and (*S*)-PCNTPA in toluene solutions under nitrogen reveal double exponential decay processes, with short mean PL lifetimes of 6.8 and 7.5 ns, respectively. Notably, apparent delayed components with extended lifetimes of 24.9 and 24.8 ns are observed under nitrogen, but get attenuated with lifetimes decreased to 6.4 and 7.9 ns under air (Fig. 2c, Supplementary Fig. 4a, and Supplementary Table 2), indicative of the involvement of triplet states in the radiative decay process. In neat films, (*S*)-PCNCP and (*S*)-PCNTPA exhibit short mean PL lifetimes of 2.8 and 3.3 ns. The reduced yet discernible delayed components are detected under nitrogen, with reduced lifetimes of 6.2 and 6.4 ns. And the lifetimes of delayed components become slightly longer upon elevating the temperature from 77 to 300 K, as unveiled by the temperature-dependent transient PL decay spectra (Supplementary Fig. 4b and 4c, and Supplementary Table 3). A similar trend is observed for these materials in doped films (Supplementary Fig. 4 and Supplementary Table 4). The fluorescence and phosphorescence spectra recorded at 77 K provide the S_1–T_1 energy splitting (ΔE_{ST}) of 0.60 and 0.47 eV for (*S*)-PCNCP and (*S*)-PCNTPA in neat films, and 0.58 and 0.40 eV in doped films (Supplementary Fig. 5). These findings reveal the absence of typical TADF property in these materials, but the delayed components with short lifetimes are likely induced by hRISC process[56], according to the theoretical calculation results.

The chiroptical properties of these chiral materials in ground state are initially investigated by using circular

https://doi.org/10.26434/chemrxiv-2024-qw671 ORCID: https://orcid.org/0000-0002-0618-6024 Content not peer-reviewed by ChemRxiv. License: CC BY 4.0

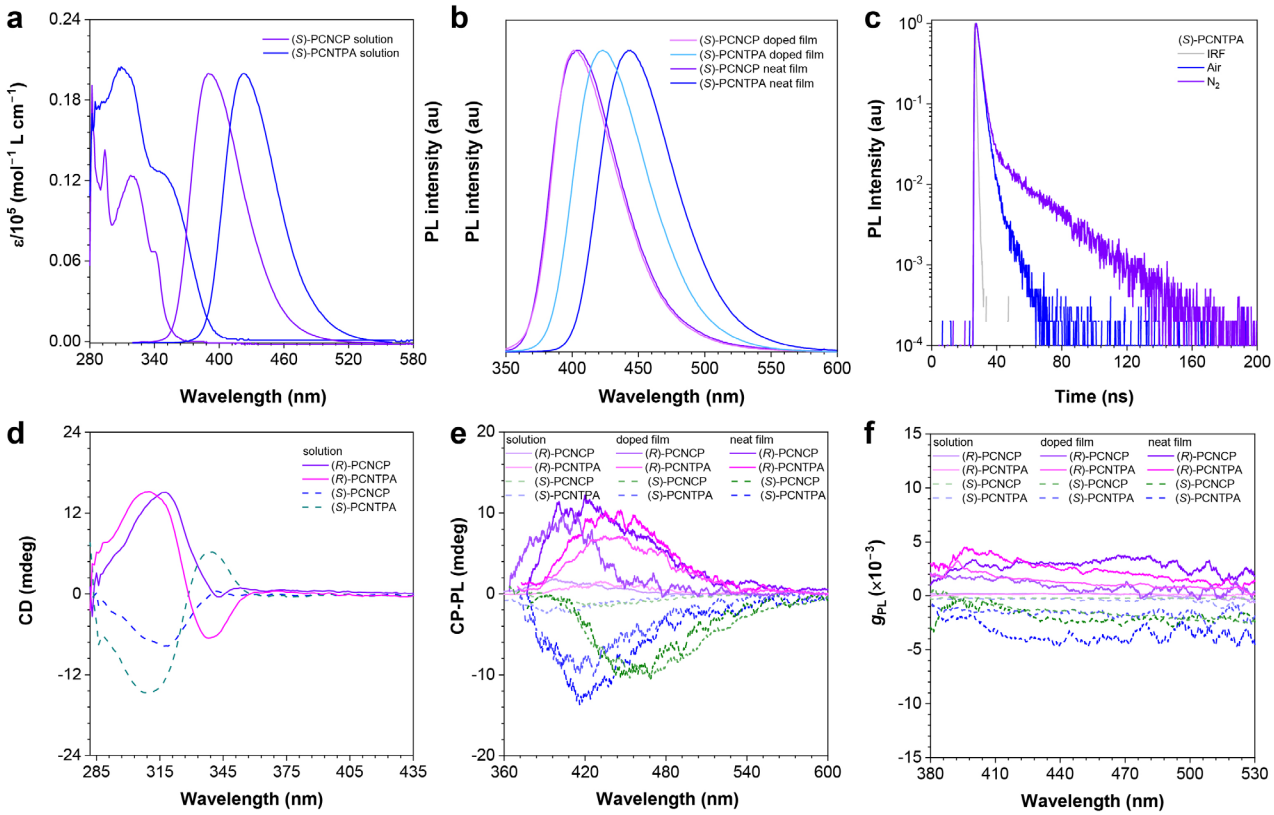

Fig. 2 | Photophysical properties and chiral properties of the chiral near-ultraviolet and deep-blue materials. a, UV-vis absorption spectra and PL spectra of (*S*)-PCNCP and (*S*)-PCNTPA in toluene solutions (1×10^{-5} M) and neat films. The excitation wavelength is 320 nm. **b**, PL spectra of (*S*)-PCNCP and (*S*)-PCNTPA in neat films and doped films (25 wt% (*S*)-/(*R*)-PCNCP in PYD-2, 40 wt% (*S*)-/(*R*)-PCNTPA in PYD-2). The excitation wavelength is 320 nm. **c**, Transient PL decay spectrum of (*S*)-PCNTPA in toluene (1×10^{-5} M). The excitation wavelength is 280 nm; IRF = instrument response function. **d**, CD spectra of (*S*)-/(*R*)-PCNCP and (*S*)-/(*R*)-PCNTPA in toluene solutions (2.0×10^{-5} M). **e**, CP-PL spectra and **f**, plots of g_{PL} value versus PL wavelength of (*S*)-/(*R*)-PCNCP and (*S*)-/(*R*)-PCNTPA in toluene (1.0×10^{-5} M), neat films, and doped films (25 wt% (*S*)-/(*R*)-PCNCP in PYD-2, 40 wt% (*S*)-/(*R*)-PCNTPA in PYD-2). The excitation wavelength is 320 nm.

dichroism (CD) spectra in dilute toluene solutions. As illustrated in Fig. 2d, the (*S*)-/(*R*)-enantiomers exhibit mirror-image bands with strong cotton effects, signifying prominent chirality. Additionally, they display distinct circularly polarized PL (CP-PL) signals in toluene solutions, confirming their chiroptical properties in excited state. For instance, (*S*)-/(*R*)-PCNTPA exhibit mirror-image CP-PL spectra with PL dissymmetry factors (g_{PL}s) of -1.80×10^{-4} and 1.26×10^{-4}, respectively. The neat films of these materials also manifest conspicuous CP-PL signals with elevated absolute g_{PL} values. Specifically, (*S*)-/(*R*)-PCNTPA in neat films exhibit g_{PL} values of -2.04×10^{-3} and 2.43×10^{-3}, respectively, better than those in doped films (-1.32×10^{-3} and 1.25×10^{-3}) (Fig. 2e and 2f, and Supplementary Table 5).

CP-EL performance

The CP-EL performances of these chiral near-ultraviolet and deep-blue materials are initially evaluated in the devices of ITO/HATCN (5 nm)/TAPC (50 nm)/TcTa (5 nm)/mCP (5 nm)/EML (20 nm)/PPF (5 nm)/TmPyPB (30 nm)/LiF (1 nm)/Al. In these devices, the doped films of the chiral near-ultraviolet and deep-blue materials function as the emitting layers (EMLs); hexaazatriphenylenehexacabonitrile (HATCN), 1,1-bis[(di-4-tolylamino)phenyl]cyclohexane (TAPC), and 2,8-bis(diphenylphosphoryl)dibenzo(b,d)furan (PPF) serve as hole-injecting, hole-transporting, and hole-blocking layers, respectively; tris(4-(carbazol-9-yl)phenyl)amine (TcTa), 1,3-di(carbazol-9-yl)benzene (*m*CP) and 1,3,5-tri(m-pyrid-3-yl-phenyl)benzene (TmPyPB) function as exciton-blocking, electron-blocking, and electron-transporting layers, respectively. All the devices exhibit excellent CP-EL

https://doi.org/10.26434/chemrxiv-2024-qw671 ORCID: https://orcid.org/0000-0002-0618-6024 Content not peer-reviewed by ChemRxiv. License: CC BY 4.0

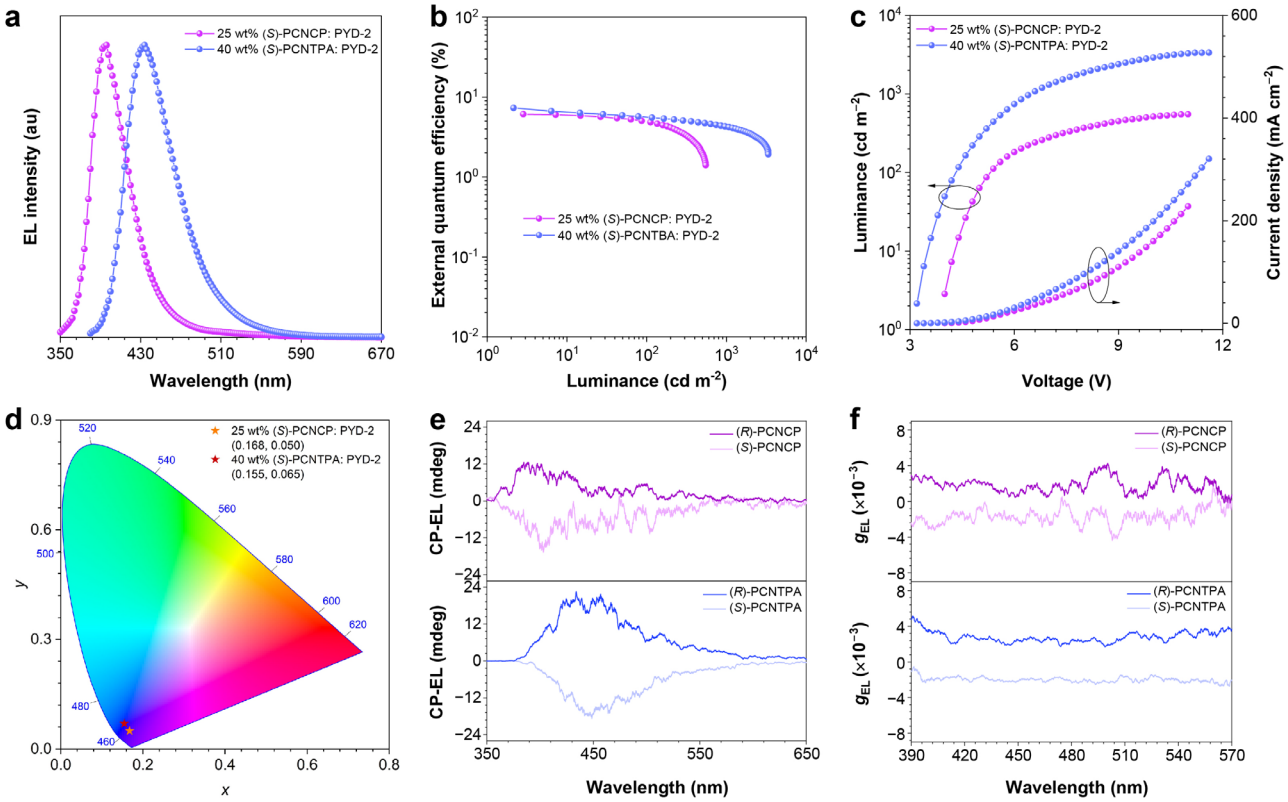

Fig. 3 | CP-EL performances of the chiral near-ultraviolet and deep-blue materials. a, EL spectra of the doped OLEDs of (*S*)-PCNCP and (*S*)-PCNTPA at 4 V. **b**, External quantum efficiency–luminance and **c**, plots of luminance–voltage–current density of the doped OLEDs. **d**, CIE color coordinates of doped OLEDs. CP-EL spectrum and plots of g_{EL} value versus EL wavelength of the doped OLEDs of **e**, (S)-PCNCP and **f**, (S)-PCNTPA. CP-EL spectra collected under 4 V.

performances, as depicted in Fig. 3 and Supplementary Fig. 6. (*S*)-PCNTPA in doped device emits deep-blue light with an EL peak at 434 nm and achieves a maximum external quantum efficiency ($\eta_{ext,max}$) of 7.3%, while (*S*)-PCNCP in doped device radiates near-ultraviolet light with an EL peak at 396 nm and a $\eta_{ext,max}$ of 6.1%. Moreover, all the (*R*)-enantiomers exhibit EL performances similar to those of the (*S*)-enantiomers (Supplementary Table 6 and Supplementary Table 7). Owing to the chiral nature, all the (*S*)-/(*R*)-enantiomers manifest good CP-EL signals, and their doped devices display mirror-image CP-EL spectra with good absolute EL dissymmetry factor ($|g_{EL}|$) values in the range of 2.02×10^{-3}–2.72×10^{-3} (Fig. 3e and 3f). In addition, these chiral materials also exhibit good CP-EL performance in nondoped OLEDs. For example, the nondoped OLED using the neat film of (*S*)-PCNTPA as EML in the same configuration shows efficient deep-blue CP-EL with a peak at 434 nm, a g_{EL} of -3.69×10^{-3} and a $\eta_{ext,max}$ of 6.0%. These results reveal that the new chiral near-ultraviolet and deep-blue materials own high potentials to construct efficient OLEDs with strong CP-EL.

CISS effect

Concerning the excellent CP-EL performance of these chiral near-ultraviolet and deep-blue materials, their CISS effect is further investigated in the device with a configuration of ITO/HATCN (5 nm)/TAPC (50 nm)/TcTa (5 nm)/mCP (5 nm)/(*S*)- or (*R*)-PCNTPA (6 nm)/30 wt% BDMAC-XT: CBP (14 nm)/TmPyPB (40 nm)/LiF (1 nm)/Al, in which the chiral deep-blue layer of (*S*)- or (*R*)-PCNTPA neat film (6 nm) and the achiral green layer of 30 wt% BDMAC-XT: CBP doped film (14 nm) are arranged as two separate layers to exclude chirality-induction effect. Additionally, a comparable device is also prepared by replacing the chiral layer with a racemized layer of 50 wt% (*S*)-PCNTPA and 50 wt% (*R*)-PCNTPA with the same thickness. As depicted in Fig. 4c and 4d, Supplementary Fig. 7a and Table 1, all of these devices display nearly identical EL peaks at 520 nm from BDMAC-XT, and outstanding

https://doi.org/10.26434/chemrxiv-2024-qw671 ORCID: https://orcid.org/0000-0002-0618-6024 Content not peer-reviewed by ChemRxiv. License: CC BY 4.0

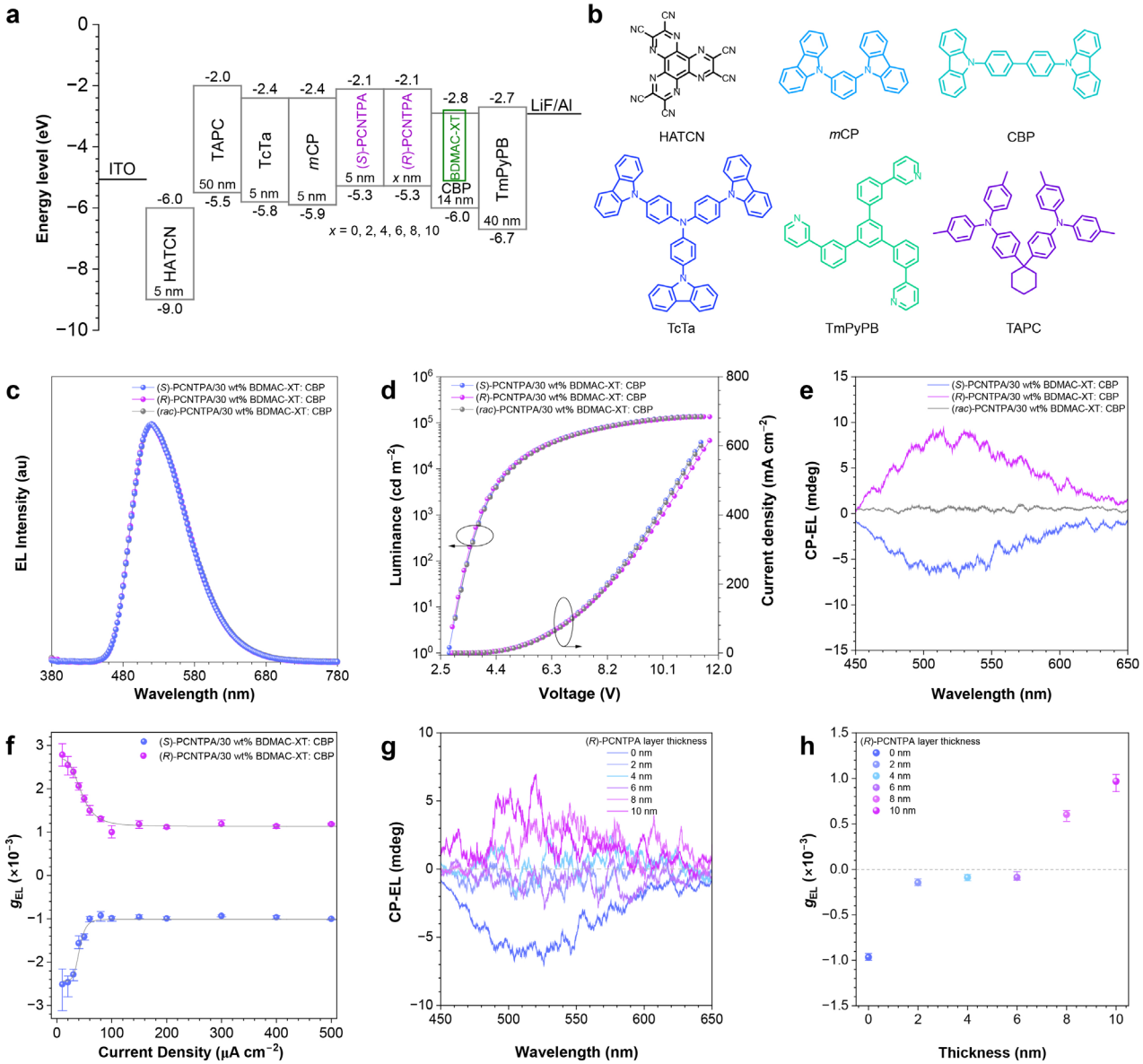

Fig. 4 | Exploration of CISS effect in green spin-OLEDs. a, Schematic diagram of device energy levels and **b**, molecular structures of the functional layers. **c**, EL spectra of the doped OLEDs at 4 V. **d**, Plots of luminance–voltage–current density and **e**, CP-EL spectra of the doped OLEDs at 4 V. **f**, g_{EL} value–current density curves of the doped OLEDs with the chiral layer of (*S*)-/(*R*)-PCNTPA. The error bars represent the standard deviations of five parallel measurements. **g**, CP-EL spectra of devices with different thickness of (*R*)-PCNTPA layer collected under 4 V. **h**, Plots of g_{EL} value versus (*R*)-PCNTPA layer thickness. The error bars represent the standard deviations of five parallel measurements.

EL performance with high luminance of up to 138400 cd m^{-2} and a notable $\eta_{ext,max}$ of 30.7%, indicative of well-balanced charge carriers and efficient exciton recombination in achiral layer of 30 wt% BDMAC-XT: CBP. Distinct CP-EL spectra peaking at around 520 with symmetrical patterns are detected, which should stem from the achiral green layers rather than the chiral (*S*)- or (*R*)-PCNTPA layers. On the contrary, no CP-EL signal is observed in the device with a racemized layer (Fig. 4e and Supplementary Fig. 7b). These results reveal that the spin-polarized charge carriers are obtained when current passes through the chiral layer, and then get recombined to generate spin-polarized excitons in achiral green layer because of the much narrower energy gap of BDMAC-XT than (*S*)-/(*R*)-PCNTPA, rendering green CP-EL from achiral BDMAC-XT.

https://doi.org/10.26434/chemrxiv-2024-qw671 **ORCID:** https://orcid.org/0000-0002-0618-6024 Content not peer-reviewed by ChemRxiv. **License:** CC BY 4.0

Previous studies demonstrated that a longer spin-dephasing time of the spin-polarized charge carriers can provide a larger g_{EL} value, and the spin-dephasing time also negatively correlates with the current density[57,58]. Therefore, with the enhancement in current density, the g_{EL} will decline to a stable value[47]. To further validate the generation of spin-polarized charge carriers in above devices, the relationship between g_{EL} and current density is investigated, and the g_{EL} values at different current densities are recorded (Fig. 3f and Supplementary Fig. 7c and 7d). It is found that the g_{EL} value of the device with the kernel layers of (*R*)-PCNTPA (6 nm)/30 wt% BDMAC-XT: CBP (14 nm) is as large as 2.78×10^{-3} when the current density is 10 μA cm^{-2}, which is decreased to 1.77×10^{-3} at 50 μA cm^{-2} and 1.18×10^{-3} at 150 μA cm^{-2}. Subsequently, along with the further increase of current density to 500 μA cm^{-2}, the g_{EL} value hovers around 1.18×10^{-3}. The device containing the layers of (*S*)-PCNTPA (6 nm)/30 wt% BDMAC-XT: CBP (14 nm) exhibits the same trend, and its g_{EL} value is reduced from -2.51×10^{-3} at 10 μA cm^{-2}, to -1.41×10^{-3} at 50 μA cm^{-2} and to -0.96×10^{-3} at 150 μA cm^{-2}, and finally stabilized at around -1.00×10^{-3} at 500 μA cm^{-2}. These findings clearly evidence the generation of spin-polarized charge carriers in the devices, proving that these organic chiral materials have CISS effect.

Theoretically, the chirality of the chiral layer has an apparent impact on the spin polarization direction of the charge carriers passing through it. When a chiral layer with (*S*)-enantiomer is located adjacent to another chiral layer with (*R*)-enantiomer, the spin polarization direction of the charge carriers should be notably influenced by altering the thickness of the chiral layers, leading to varied CP-EL signals. Thereby, to have a deeper understanding on how the CISS effect of the chiral layer influences the CP-EL property of the achiral layer, a set of experiments involving modulations on the chirality and thickness of the chiral layer are conducted. The device configuration is designed as ITO/HATCN (5 nm)/TAPC (50 nm)/TcTa (5 nm)/mCP (5 nm)/(*S*)-PCNTPA (6 nm)/(*R*)-PCNTPA (*x* nm)/30 wt% BDMAC-XT: CBP (14 nm)/TmPyPB (40 nm)/LiF (1 nm)/Al (Fig. 3a and 3b), where the thickness of (*S*)-PCNTPA layer is set as 6 nm, while that of (*R*)-PCNTPA layer is altered progressively (x = 0, 2, 4, 6, 8 and 10). When x is 0, the device shows an apparent CP-EL signal, with a g_{EL} value of -1.0×10^{-3}, consistent with the previous results. However, for x = 2, 4 and 6, the devices exhibit almost no CP-EL signals because of the opposite interference of the chiral layers with opposite chirality, by which the spin polarization direction of charge carriers becomes randomized as current traverses through two chiral layers with opposite chirality, (*S*)-PCNTPA/(*R*)-PCNTPA. Significantly, when x is increased to 8 and 10, the devices display evident opposite CP-EL signals in comparison with that at x = 0 (Fig. 3g and 3h, and Supplementary Fig. 7e). This outcome indicates that the spin polarization direction of charge carriers is realigned when passing through the thicker (*R*)-PCNTPA chiral layer, leading to the flip of the CP-EL signals. The obvious switch in the g_{EL} value from negative to positive as the thickness of the (*R*)-PCNTPA chiral layer increases proves that the green CP-EL of achiral layer is triggered by the spin-polarized charge carriers generated by the chiral layer, and offers further evidence for the CISS effect of (*S*)-/(*R*)-PCNTPA chiral materials.

Spin-polarized WOLEDs

The above inspiring results encourage us to figure out whether this CISS effect is applicable to more complex systems with multiple achiral layers in WOLEDs. Herein, the (*S*)-/(*R*)-PCNTPA chiral layer plus two achiral layers containing red DBP and green BDMAC-XT, respectively, are utilized to construct spin-polarized WOLEDs (spin-WOLEDs). The configuration of such three-emitting-layer WOLED (W1) is designed as ITO/HATCN (5 nm)/TAPC (50 nm)/1 wt% DBP: TcTa (5 nm)/30 wt% BDMAC-XT: CBP (3 nm)/40 wt% (*S*)-PCNTPA: PYD-2 (12 nm)/TmPyPB (40 nm)/LiF (1 nm)/Al (Fig. 5a). In comparison with the green spin-OLEDs discussed above, the configuration of this spin-WOLED is adjusted, considering that the blue emission of chiral layer is needed as one of three primary colors for white light. In green spin-OLEDs, owing to the dominative hole-transporting nature of (*S*)-/(*R*)-PCNTPA, the chiral deep-blue layer is placed at the hole injection region, and the holes can be easily transported from the hole injection and transport layers to the chiral deep-blue layer, and then to the achiral green layer. The exciton recombination occurs in the achiral green layer to generate green EL, and the bipolar host material (CBP) of the green

https://doi.org/10.26434/chemrxiv-2024-qw671 ORCID: https://orcid.org/0000-0002-0618-6024 Content not peer-reviewed by ChemRxiv. License: CC BY 4.0

Table 1 | EL performances of the OLEDs based on new chiral materials. [a)]

EML	V_{on} (V)	λ_{EL} (nm)	L_{max} (cd m^{-2})	$\eta_{C,max}$ (cd A^{-1})	$\eta_{P,max}$ (lm W^{-1})	$\eta_{ext,max}$ (%)	CIE (x, y)	CRI	g_{EL} (10^{-3})
(*S*)-PCNTPA	3.6	434	2127	3.7	3.1	6.0	(0.157, 0.073)	-	–3.69
25 wt% (*S*)-PCNCP: PYD-2	3.9	396	552	1.1	0.8	6.1	(0.168, 0.050)	-	–2.64
40 wt% (*S*)-PCNTPA: PYD-2	3.1	434	3355	4.0	3.9	7.3	(0.155, 0.065)	-	–2.02
EML-G1	2.8	520	138400	97.1	101.6	30.4	(0.293, 0.568)	-	–1.00
EML-G2	2.8	520	134600	98.1	104.2	30.7	(0.293, 0.567)	-	1.18
EML-G3	2.9	520	134200	95.2	99.6	29.8	(0.293, 0.569)	-	null
EML-W1	3.1		4553	49.1	48.2	24.2	(0.321, 0.339)	92	5.50
EML-W2	3.1		3051	43.9	43.1	20.6	(0.253, 0.259)	94	4.55
EML-W3	2.8		6273	39.6	41.5	20.9	(0.373, 0.409)	91	-
EML-W4	2.9		5453	55.7	58.4	26.6	(0.339, 0.433)	90	5.26

[a)] Abbreviations: V_{on} = turn-on voltage at 1 cd m^{-2}; $\eta_{C,max}$ = maximum current efficiency; $\eta_{P,max}$ = maximum power efficiency; $\eta_{ext,max}$ = maximum external quantum efficiency; L_{max} = maximum luminance; CIE = Commission International de I'Eclairage coordinates; λ_{EL} = EL peak. EML: light-emitting layer. EML-G1: (*S*)-PCNTPA (6 nm)/30 wt% BDMAC-XT: CBP (14 nm); EML-G2: (*R*)-PCNTPA (6 nm)/30 wt% BDMAC-XT: CBP (14 nm); EML-G3: (*rac*)-PCNTPA (6 nm)/30 wt% BDMAC-XT: CBP (14 nm); EML-W1: 1 wt% DBP: TcTa (5 nm)/30 wt% BDMAC-XT: CBP (3 nm)/40 wt% (*R*)-PCNTPA: PYD-2 (12 nm); EML-W2: 1 wt% DBP: TcTa (5 nm)/30 wt% BDMAC-XT: CBP (3 nm)/TcTa (2 nm)/40 wt% (*S*)-PCNTPA: PYD-2 (12 nm); EML-W3: 1 wt% DBP: TcTa (4 nm)/30 wt% BDMAC-XT: CBP (3 nm)/20 wt% DMAC-DPS: DPEPO (2 nm)/40 wt% (*S*)-PCNTPA: PYD-2 (10 nm); EML- W4: 1 wt% DBP: TcTa (5 nm)/30 wt% BDMAC-XT: CBP (3 nm)/20 wt% DMAC-DPS: DPEPO (2 nm)/25 wt% (*S*)-PCNTPA: PYD-2 (10 nm).

layer also facilitates the exciton recombination in this layer. While in spin-WOLEDs, given the dominative electron-transporting nature of PYD-2 host, the chiral deep-blue layer is placed in the electron injection region to enhance exciton recombination in this layer for obtaining deep-blue emission. In addition, the bipolar CBP host can enhance the transport of electrons and holes, which broadens the exciton recombination zone to the adjacent achiral red layer. Thus, in spin-WOLEDs, it is envisioned that the spin-polarized charge carriers can get recombined in green, red and deep-blue layers simultaneously to yield white light with CP-EL signals.

Successfully, unlike two-emitting-layer devices with single CP-EL signal from green BDMAC-XT layer, the three-emitting-layer device W1 display white CP-EL signals consisting of green and red CP-EL emissions from achiral BDMAC-XT and DBP, respectively, as well as deep-blue emission from chiral (*S*)-PCNTPA. Specifically, the EL spectrum of device W1 shows three EL peaks at 434 nm from (*S*)-PCNTPA layer, 510 nm from BDMAC-XT layer, and 610 nm from DBP layer, with a high color rendering index (CRI) of 92, and the good chromaticity coordinates are (0.321, 0.339), indicative of the high quality of the white light (Fig. 5c-5e, Supplementary Fig. 8a). Device W1 also exhibits excellent performance with a high $\eta_{ext,max}$ reaching 24.2% (Table 1). More importantly, apparent CP-EL signals covering a wide region from 380 to 780 nm with $|g_{EL}|$ values of 0.47×10^{-3} @ 434 nm, 3.51×10^{-3} @510 nm and 1.90×10^{-3} @610 nm are recorded, revealing both achiral green and red layers have been enabled to radiate CP-EL in device W1 (Supplementary Fig. 8b and 8c), indicating the CISS effect still works in multi-emitting-layer devices.

To further confirm the CISS effect in WOLEDs and enhance device performance as well, the device configuration is optimized as ITO/HATCN (5 nm)/TAPC (50 nm)/1 wt% DBP: TcTa (5 nm)/30 wt% BDMAC-XT: CBP (3 nm)/TcTa (2 nm)/40 wt% (*S*)-PCNTPA: PYD-2 (12 nm)/TmPyPB (40 nm)/LiF (1 nm)/Al (device W2). In comparison with device W1, device W2 has a supplementary TcTa layer between the chiral deep-blue layer and achiral green layer for completely eliminating the chirality-induction effect and validating the CISS effect. Encouragingly, device W2 achieves pure white light with an excellent CRI of 94 and good CIE coordinates of (0.253, 0.259), as well as a remarkable $\eta_{ext,max}$ of 20.4%. The EL spectrum of device W2 is similar to that of device W1,

https://doi.org/10.26434/chemrxiv-2024-qw671 **ORCID:** https://orcid.org/0000-0002-0618-6024 Content not peer-reviewed by ChemRxiv. **License:** CC BY 4.0

displaying three main EL peaks at 434, 510 and 610 nm, respectively, but the EL intensity in blue region is increased. Device W2 also shows obvious CP-EL signals in a wide region from 380 to 780 nm with g_{EL} values of -3.26×10^{-3} @434 nm, -3.86×10^{-3} @510 nm and -2.92×10^{-3} @610 nm, and the CP-EL signal in blue region is also strengthened to some degree relative to that of device W1 (Fig. 5f). The achiral TcTa layer in device W2 functions as exciton- and electron-blocking layer between chiral deep-blue layer and achiral green layer, leading to enhanced exciton recombination in chiral deep-blue layer, and thus increased signals in both EL and CP-EL spectra. Since the achiral green BDMAC-XT layer is located adjacent to the achiral TcTa layer, then to the chiral deep-blue (*S*)-PCNTPA

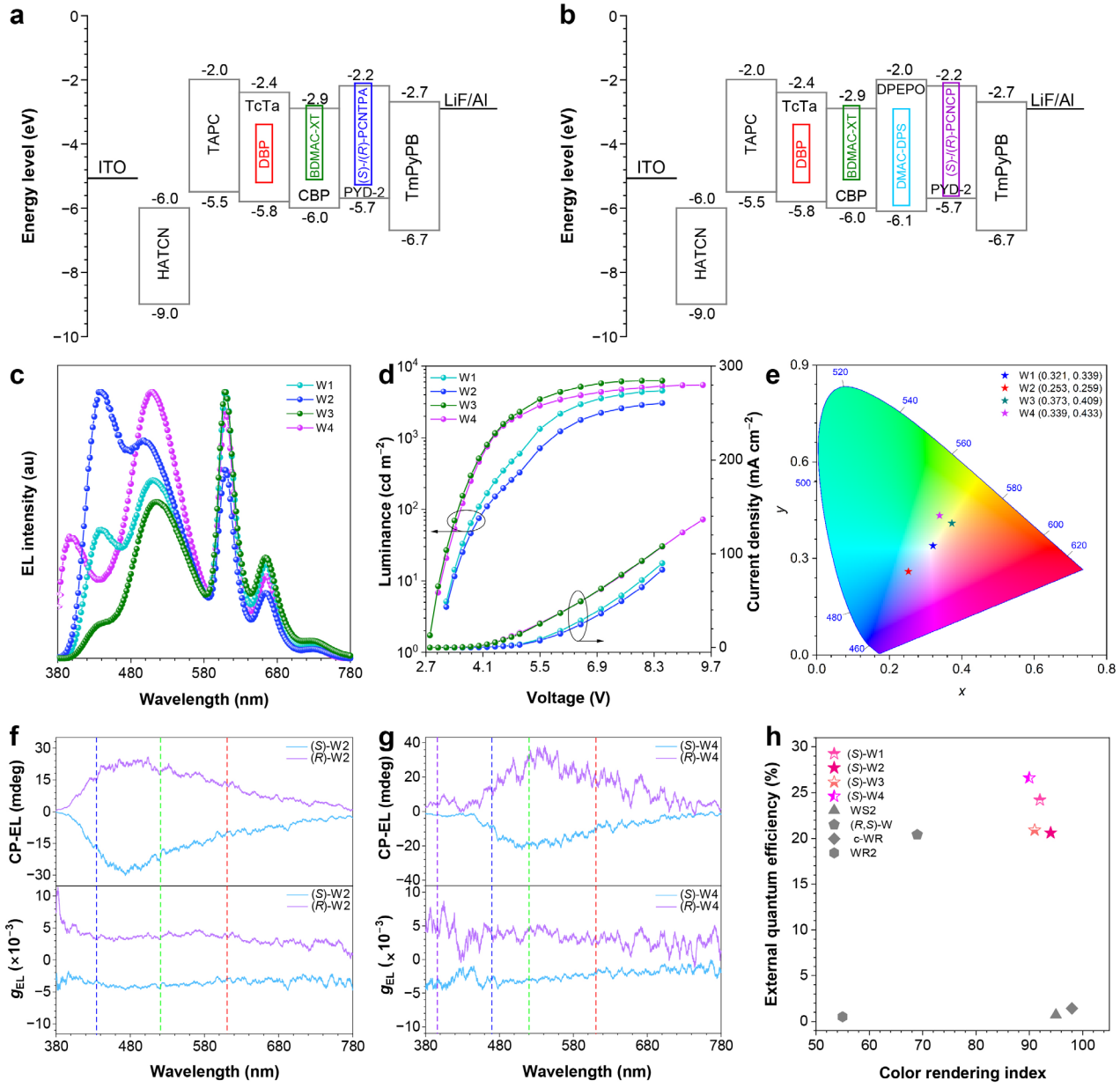

Fig. 5 | Exploration of CISS effect in spin-WOLEDs. Schematic diagram of configurations and energy levels of **a**, three-emitting-layer spin-WOLEDs and **b,** four-emitting-layer spin-WOLEDs. **c**, EL spectra of devices W1, W2, W3 and W4 at 1000 cd m^{-2}. **d**, Plots of luminance–voltage–current density of spin-WOLEDs. **e**, CIE color coordinates of spin-WOLEDs at 1000 cd m^{-2}. CP-EL spectra and plots of g_{EL} value versus EL wavelength of **f**, device W1 and **g**, device W4. CP-EL spectra collected at 4 V. **h**, Reported external quantum efficiencies and color rendering index of circularly polarized WOLEDs in the literature. (*S*)/(*R*) indicate (*S*)-/(*R*)-enantiomers used in the devices.

https://doi.org/10.26434/chemrxiv-2024-qw671 **ORCID:** https://orcid.org/0000-0002-0618-6024 Content not peer-reviewed by ChemRxiv. **License:** CC BY 4.0

layer, the observed green CP-EL signal should not be caused by the chiral environment induced by the chiral blue (*S*)-PCNTPA layer. Furthermore, the achiral red DBP layer is situated next to the achiral green BDMAC-XT layer in device W2, namely it also has zero contact with the chiral deep-blue (*S*)-PCNTPA layer. Therefore, the observed red CP-EL signal should be attributed to the spin-polarized excitons rather than the chiral environment as well. These findings provide further evidences for that spin-polarized charge carriers are acquired when current passes through the chiral (*S*)-PCNTPA layer, and then are transported into achiral green and red layers to form spin-polarized excitons, ultimately furnishing green and red CP-EL signals (Fig. 5f).

Finally, this strategy is applied to a more complex system of four-emitting-layer spin-WOLED with a configuration of ITO/HATCN (5 nm)/TAPC (50 nm)/1 wt% DBP: TcTa (4 nm)/30 wt% BDMAC-XT: CBP (3 nm)/20 wt% DMAC-DPS: DPEPO (2 nm)/40 wt% (*S*)-PCNTPA: PYD-2 (10 nm)/TmPyPB (30 nm)/LiF (1 nm)/Al (device W3). Delightfully, device W3 also achieves efficient white EL with a high $\eta_{ext,max}$ of 20.9%, an excellent CRI of 91, good CIE coordinates of (0.373, 0.409), and apparent CP-EL signals. The EL peak of DMAC-DPS is located at 469 nm, close to that of (*S*)-PCNTPA (434 nm), which may make it difficult to distinguish the CP-EL signals of these two layers. Thus, to better display the CISS effect, the chiral near-ultraviolet (*S*)-PCNCP material is employed to fabricate another four-emitting-layer spin-WOLED (device W4) with a configuration of ITO/HATCN (5 nm)/TAPC (50 nm)/1 wt% DBP: TcTa (5 nm)/30 wt% BDMAC-XT: CBP (3 nm)/20 wt% DMAC-DPS: DPEPO (2 nm)/25 wt% (*S*)-PCNTPA: PYD-2 (10 nm)/TmPyPB (30 nm)/LiF (1 nm)/Al (Fig. 5b). Device W4 shows a broad EL spectrum containing multiple EL peaks with a high CRI of 90 and CIE coordinates of (0.339, 0.433). Prominent CP-EL signals are recorded with g_{EL} values of -3.08×10^{-3} @396 nm from (*S*)-PCNCP layer, -2.88×10^{-3} @469 nm from DMAC-DPS layer, -3.52×10^{-3} @510 nm from BDMAC-XT layer and -2.05×10^{-3}@610 nm from DBP layer, respectively (Fig. 5g), revealing that all the three achiral layers have generated CP-EL emissions simultaneously. Meanwhile, an outstanding $\eta_{ext,max}$ of 26.6% is attained by device W4, confirming the success of the complex four-emitting-layer spin-WOLED. The remarkable CP-EL performance indicates that device W4 is the most efficient OLED with circularly polarized white light reported so far (Fig. 5h and Supplementary Table 9)[59-62].

Discussion

In summary, a novel strategy for achieving efficient CP-EL is proposed based on CISS effect for the first time. Initially, robust chiral near-ultraviolet ((*S*)-/(*R*)-PCNCP) and deep-blue ((*S*)-/(*R*)-PCNTPA) materials with wide energy gaps are explored, which provide highly efficient near-ultraviolet and deep-blue CP-EL with good $|g_{EL}|$ values of up to 3.76×10^{-3} and outstanding $\eta_{ext,max}$s of 6.1% @ 396 nm and 7.3% @ 434 nm. Then, efficient green spin-OLEDs with excellent $\eta_{ext,max}$s reaching 31.5 % and $|g_{EL}|$ values around 1.00×10^{-3} are obtained by aligning the chiral deep-blue (*S*)-PCNTPA layer to the achiral green layer. It is rationalized that these new chiral materials have prominent CISS effect, and spin-polarized charge carriers are generated when the current traverses through these chiral deep-blue layer, which get recombined to yield spin-polarized excitons in achiral green layer, resulting in green CP-EL. The presence of spin-polarized charge carriers is validated by the changes in g_{EL} values at different current densities and by the chirality flip via modulating the chirality and thickness of the chiral layers. Finally, the CISS effect and spin-polarized charge carriers are further demonstrated in more complex three-emitting-layer and four-emitting-layer spin-WOLEDs by incorporating multiple achiral sky-blue, orange and red layers with chiral near-ultraviolet or deep-blue layers. The spin-polarized charge carriers generated from chiral layers can form spin-polarized excitons in achiral sky-blue, green and red layers simultaneously, leading to sky-blue, green and red CP-EL emissions. In consequence, highly efficient spin-WOLEDs are realized, providing strong circularly polarized white light with outstanding $\eta_{ext,max}$ of 26.6%, $|g_{EL}|$ of 5.50×10^{-3} and CRI of 94, much superior to the performances of circularly polarized WOLEDs in the literature. These results prove the applicability and feasibility of the proposed approach for realizing efficient white CP-EL based on CISS effect from a single organic chiral layer, paving a novel and effective avenue towards OLEDs with high-quality circularly polarized white light.

https://doi.org/10.26434/chemrxiv-2024-qw671 **ORCID:** https://orcid.org/0000-0002-0618-6024 Content not peer-reviewed by ChemRxiv. **License:** CC BY 4.0

Data availability

The data that support the findings of this study are available from the corresponding authors on request. All data generated or analyzed during this study are included in this published article and its Supplementary Information.

References

1 Brandt, J. R., Salerno, F. & Fuchter, M. J. The added value of small-molecule chirality in technological applications. *Nat. Rev. Chem.* **1**, 0045 (2017).

2 Imai, Y., Nakano, Y., Kawai, T. & Yuasa, J. A smart sensing method for object identification using circularly polarized luminescence from coordination-driven self-assembly. *Angew. Chem. Int. Ed.* **57**, 8973-8978 (2018).

3 MacKenzie, L. E. & Pal, R. Circularly polarized lanthanide luminescence for advanced security inks. *Nat. Rev. Chem.* **5**, 109-124 (2021).

4 Adewuyi, J. A. & Ung, G. High quantum yields from perfluorinated binolate erbium complexes and their circularly polarized luminescence. *J. Am. Chem. Soc.* **146**, 7097-7104 (2024).

5 Liu, N., Gao, R. T. & Wu, Z. Q. Helix-induced asymmetric self-assembly of π-conjugated block copolymers: from controlled syntheses to distinct properties. *Acc. Chem. Res.* **56**, 2954-2967 (2023).

6 Sang, Y., Han, J., Zhao, T., Duan, P. & Liu, M. Circularly polarized luminescence in nanoassemblies: generation, amplification, and application. *Adv. Mater.* **32**, 1900110 (2019).

7 Zhang, D. W., Li, M. & Chen, C. F. Recent advances in circularly polarized electroluminescence based on organic light-emitting diodes. *Chem. Soc. Rev.* **49**, 1331-1343 (2020).

8 Liao, X. J. *et al.* Planar chiral multiple resonance thermally activated delayed fluorescence materials for efficient circularly polarized electroluminescence. *Angew. Chem. Int. Ed.* **62**, e202217045 (2023).

9 Yang, S. Y. *et al.* Circularly polarized thermally activated delayed fluorescence emitters in through-space charge transfer on asymmetric spiro skeletons. *J. Am. Chem. Soc.* **142**, 17756-17765 (2020).

10 Wu, X. *et al.* Fabrication of circularly polarized MR-TADF emitters with asymmetrical peripheral-lock enhancing helical B/N-doped nanographenes. *Adv. Mater.* **34**, e2105080 (2022).

11 Matsumura, K., Inoue, R. & Morisaki, Y. Optically active a-shaped cyclic molecules based on planar chiral [2.2]paracyclophanes emitting bright circularly polarized luminescence with high anisotropy factors. *Adv. Funct. Mater.* **33**, 2310566 (2023).

12 Dhbaibi, K. *et al.* Low-temperature luminescence in organic helicenes: singlet versus triplet state circularly polarized emission. *J. Phys. Chem. Lett.* **14**, 1073-1081 (2023).

13 Geng, Z. *et al.* Inverted and amplified CP-EL behavior promoted by AIE-active chiral co-assembled helical nanofibers. *Adv. Mater.* **34**, e2209495 (2022).

14 Chen, Z. *et al.* High-performance circularly polarized electroluminescence with simultaneous narrowband emission, high efficiency, and large dissymmetry factor. *Adv. Mater.* **34**, e2109147 (2022).

15 Dong, Q. *et al.* A chiral bipolar host for efficient solution-processed circularly polarized OLEDs via a chirality energy transfer process. *Chem. Commun.* **60**, 3421-3424 (2024).

16 Frédéric, L. *et al.* Maximizing chiral perturbation on thermally activated delayed fluorescence emitters and elaboration of the first top-emission circularly polarized OLED. *Adv. Funct. Mater.* **30**, 2004838 (2020).

17 Zinna, F., Giovanella, U. & Di Bari, L. Highly circularly polarized electroluminescence from a chiral europium complex. *Adv. Mater.* **27**, 1791-1795 (2015).

18 Crassous, J. *et al.* Materials for chiral light control. *Nat. Rev. Mater.* **8**, 365-371 (2023).

19 Yang, W. *et al.* Chiral peropyrene: synthesis, structure, and properties. *J. Am. Chem. Soc.* **139**, 13102-13109 (2017).

20 Wang, Y. J., Shi, X. Y., Xing, P., Dong, X. Y. & Zang, S. Q. Halogen bonding-driven chiral amplification of a bimetallic gold-copper cluster through hierarchical assembly. *Sci. Adv.* **9**, eadj9013 (2023).

https://doi.org/10.26434/chemrxiv-2024-qw671 **ORCID:** https://orcid.org/0000-0002-0618-6024 Content not peer-reviewed by ChemRxiv. **License:** CC BY 4.0

21 Wan, L., Liu, Y., Fuchter, M. J. & Yan, B. Anomalous circularly polarized light emission in organic light-emitting diodes caused by orbital–momentum locking. *Nat. Photon.* **17**, 193-199 (2022).
22 Medel, M. A. *et al.* Octagon-embedded carbohelicene as a chiral motif for circularly polarized luminescence emission of saddle-helix nanographenes. *Angew. Chem. Int. Ed.* **60**, 6094-6100 (2021).
23 Takaishi, K., Murakami, S., Yoshinami, F. & Ema, T. Binaphthyl-bridged pyrenophanes: intense circularly polarized luminescence based on a D_2 symmetry strategy. *Angew. Chem. Int. Ed.* **61**, e202204609 (2022).
24 Zhang, L., Wang, T., Jiang, J. & Liu, M. Chiral porphyrin assemblies. *Aggregate* **4**, e198 (2022).
25 Naaman, R., Paltiel, Y. & Waldeck, D. H. Chiral molecules and the electron spin. *Nat. Rev. Chem.* **3**, 250-260 (2019).
26 Adhikari, Y. *et al.* Interplay of structural chirality, electron spin and topological orbital in chiral molecular spin valves. *Nat. Commun.* **14**, 5163 (2023).
27 Rahman, M. W. *et al.* Chirality-induced spin selectivity in heterochiral short-peptide-carbon-nanotube hybrid networks: role of supramolecular chirality. *ACS Nano* **16**, 16941-16953 (2022).
28 Huizi-Rayo, U. *et al.* An ideal spin filter: long-range, high-spin selectivity in chiral helicoidal 3-dimensional metal organic frameworks. *Nano Lett.* **20**, 8476-8482 (2020).
29 Ozturk, S. F. & Sasselov, D. D. On the origins of life's homochirality: Inducing enantiomeric excess with spin-polarized electrons. *Proc. Natl. Acad. Sci. U.S.A.* **119**, e2204765119 (2022).
30 Shang, Z. *et al.* Chiral-molecule-based spintronic devices. *Small* **18**, e2203015 (2022).
31 Evers, F. *et al.* Theory of chirality induced spin selectivity: progress and challenges. *Adv. Mater.* **34**, e2106629 (2022).
32 Ko, C. H. *et al.* Twisted molecular wires polarize spin currents at room temperature. *Proc. Natl. Acad. Sci. U.S.A.* **119**, e2116180119 (2022).
33 Yang, X., van der Wal, C. H. & van Wees, B. J. Detecting chirality in two-terminal electronic nanodevices. *Nano Lett.* **20**, 6148-6154 (2020).
34 Aizawa, H. *et al.* Enantioselectivity of discretized helical supramolecule consisting of achiral cobalt phthalocyanines via chiral-induced spin selectivity effect. *Nat. Commun.* **14**, 4530 (2023).
35 Fiederling, R. *et al.* Injection and detection of a spin-polarized current in a light-emitting diode. *Nature* **402**, 787-790 (1999).
36 Farshchi, R., Ramsteiner, M., Herfort, J., Tahraoui, A. & Grahn, H. T. Optical communication of spin information between light emitting diodes. *Appl. Phys. Lett.* **98**, 162508 (2011).
37 Chiesa, A. *et al.* Chirality-induced spin selectivity: An enabling technology for quantum applications. *Adv. Mater.* **35**, e2300472 (2023).
38 Metzger, T. S. *et al.* Dynamic spin-controlled enantioselective catalytic chiral reactions. *J. Phys. Chem. Lett.* **12**, 5469-5472 (2021).
39 Dianat, A. *et al.* Role of exchange interactions in the magnetic response and intermolecular recognition of chiral molecules. *Nano Lett.* **20**, 7077-7086 (2020).
40 Bloom, B. P. *et al.* Asymmetric reactions induced by electron spin polarization. *Phys. Chem. Chem. Phys.* **22**, 21570-21582 (2020).
41 Bangruwa, N. *et al.* Chiral-induced spin selectivity modulated time-correlated single-photon counting for DNA hybridization detection. *J. Phys. Chem. Lett.* **15**, 2384-2391 (2024).
42 Mondal, P. C., Mtangi, W. & Fontanesi, C. Chiro-spintronics: spin-dependent electrochemistry and water splitting using chiral molecular films. *Small Methods* **2**, 1700313 (2018).
43 Bai, T., Ai, J., Duan, Y., Han, L. & Che, S. Spin selectivity of chiral mesostructured iron oxides with different magnetisms. *Small* **18**, e2104509 (2022).

https://doi.org/10.26434/chemrxiv-2024-qw671 **ORCID:** https://orcid.org/0000-0002-0618-6024 Content not peer-reviewed by ChemRxiv. **License:** CC BY 4.0

44 Nishizawa, N., Nishibayashi, K. & Munekata, H. Pure circular polarization electroluminescence at room temperature with spin-polarized light-emitting diodes. *Proc. Natl. Acad. Sci. U.S.A.* **114**, 1783-1788 (2017).
45 Holub, M. & Bhattacharya, P. Spin-polarized light-emitting diodes and lasers. *J. Phys. D: Appl. Phys.* **40**, R179-R203 (2007).
46 Bloom, B. P., Paltiel, Y., Naaman, R. & Waldeck, D. H. Chiral induced spin selectivity. *Chem. Rev.* **124**, 1950-1991 (2024).
47 Kim, Y. H. *et al.* Chiral-induced spin selectivity enables a room-temperature spin light-emitting diode. *Science* **371**, 1129-1133 (2021).
48 Mustaqeem, M. *et al.* Solution-processed and room-temperature spin light-emitting diode based on quantum dots/chiral metal-organic framework heterostructure. *Adv. Funct. Mater.* **33**, 2213587 (2023).
49 Lu, H., Vardeny, Z. V. & Beard, M. C. Control of light, spin and charge with chiral metal halide semiconductors. *Nat. Rev. Chem.* **6**, 470-485 (2022).
50 Eckvahl, H. J. *et al.* Direct observation of chirality-induced spin selectivity in electron donor-acceptor molecules. *Science* **382**, 197-201 (2023).
51 Nakajima, R. *et al.* Giant spin polarization and a pair of antiparallel spins in a chiral superconductor. *Nature* **613**, 479-484 (2023).
52 Gao, M. & Qin, W. Organic chiral spin-optics: The interaction between spin and photon in organic chiral materials. *Adv. Optical Mater.* **9**, 2101201 (2021).
53 Han, C. *et al.* Ladder-like energy-relaying exciplex enables 100% internal quantum efficiency of white TADF-based diodes in a single emissive layer. *Nat. Commun.* **12**, 3640 (2021).
54 Yang, M., Park, I. S. & Yasuda, T. Full-color, narrowband, and high-efficiency electroluminescence from boron and carbazole embedded polycyclic heteroaromatics. *J. Am. Chem. Soc.* **142**, 19468-19472 (2020).
55 Chen, J. *et al.* Versatile aggregation-enhanced delayed fluorescence luminogens functioning as emitters and hosts for high-performance organic light-emitting diodes. *CCS Chem.* 230-240 (2021).
56 Chen, J. *et al.* Robust luminescent molecules with high-level reverse intersystem crossing for efficient near ultraviolet organic light-emitting diodes. *Angew. Chem. Int. Ed.* **61**, e202116810 (2022).
57 Scharff, T. *et al.* Complete polarization of electronic spins in OLEDs. *Nat. Commun.* **12**, 2071 (2021).
58 Wang, J. *et al.* Spin-optoelectronic devices based on hybrid organic-inorganic trihalide perovskites. *Nat. Commun.* **10**, 129 (2019).
59 Zhang, Y., Jing, T., Quan, Y., Ye, S. & Cheng, Y. Standard white CP-OLEDs performance achieved by intramolecular chirality transfer mechanism through polymer chain. *Adv. Optical Mater.* **10**, 2200915 (2022).
60 Zhang, Y., Li, J., Quan, Y., Ye, S. & Cheng, Y. Solution-processed white circularly polarized organic light-emitting diodes based on chiral binaphthyl emitters. *Chem. Eur. J.* **27**, 589-593 (2021).
61 Zhang, Y. P. *et al.* Circularly polarized white organic light-emitting diodes based on spiro-type thermally activated delayed fluorescence materials. *Angew. Chem. Int. Ed.* **61**, e202200290 (2022).
62 Zhang, Y., Li, Y. P., Quan, Y. W., Ye, S. H. & Cheng, Y. X. Remarkable white circularly polarized electroluminescence based on chiral co-assembled helix nanofiber emitters. *Angew. Chem. Int. Ed.* **62**, e202214424 (2023).

Methods

General information

All the synthesis experiments were performed under nitrogen atmosphere. All the chemicals and reagents were purchased from commercial sources and used as received without further purification. The final products were subjected to vacuum sublimation to further improve purity before PL and EL properties investigations. NMR spectra were measured on a Bruker Avance-500 spectrometer in the solvents indicated.

https://doi.org/10.26434/chemrxiv-2024-qw671 **ORCID:** https://orcid.org/0000-0002-0618-6024 Content not peer-reviewed by ChemRxiv. **License:** CC BY 4.0

High-resolution mass spectra (HRMS) were recorded on a GCT premier CAB048 mass spectrometer operating in MALDI-TOF mode. Cyclic voltammograms were measured in a solution of tetra-*n*-butylammonium hexafluorophosphate (Bu_4NPF_6, 0.1 M) in dichloromethane or *N*,*N*-dimethylformamide containing the sample at a scan rate of 50 mV s^{-1}. Three-electrode system (Ag/Ag^+, platinum wire and glassy carbon electrode as reference, counter and work electrode, respectively) was used in cyclic voltammetry measurement to determine HOMO energy levels (HOMO = –[E_{ox} + 4.8] eV; LUMO = HOMO + E_g; E_{ox} and E_g represent the onset oxidation potential relative to ferrocene and optical energy gap, respectively. The ground-state geometries were optimized using the density function theory (DFT) method with M06-2X functional at the basis set level of 6-31G (d,p). All the calculations were performed using Gaussian16 package.

Photophysical property measurement

UV-vis absorption spectra were measured on a Shimadzu UV-2600 spectrophotometer. PL spectra were recorded on a Horiba Fluoromax-4 spectrofluorometer. Fluorescence quantum yields were measured using a Hamamatsu absolute PL quantum yield spectrometer C11347 Quantaurus QY. Transient PL decay spectra were measured under nitrogen atmosphere (solution) or vacuum (neat film), using Quantaurus-Tau fluorescence lifetime measurement system (C11367-03, Hamamatsu Photonics Co., Japan). Circular dichroism (CD) spectra were recorded with a Chirascan spectrometer (Applied Photophysics, England). Circularly polarized photoluminescence (CP-PL) and circularly polarized electroluminescence (CP-EL) spectra were recorded at 100 nm min^{-1} scan speed with a commercialized instrument JASCO CPL-300 at room temperature.

OLED fabrication and characterization

Glass substrates pre-coated with a 90-nm-thin layer of indium tin oxide (ITO) with a sheet resistance of 20 Ω per square were thoroughly cleaned for 10 minutes in ultrasonic bath of acetone, isopropyl alcohol, detergent, deionized water, and isopropyl alcohol, and then treated with O_2 plasma for 5 min in sequence. Organic layers were deposited onto the ITO-coated substrates by high-vacuum (< 5×10^{-4} Pa) thermal evaporation. Deposition rates were controlled by independent quartz crystal oscillators, which are 1~2 Å s^{-1} for organic materials, 0.2 Å s^{-1} for LiF, and 5 Å s^{-1} for Al, respectively. The emission area of the device is 3 × 3 mm^2 as shaped by the overlapping area of the anode and cathode. All the device characterization steps were carried out at room temperature under ambient laboratory conditions without encapsulation. The luminance–voltage–current density characteristics and EL spectra for monochromatic OLEDs were measured in a dual-channel Keithley 2614B source meter and a PIN-25D silicon photodiode. The luminance–voltage–current density characteristics and EL spectra of all the WOLEDs were measured in a PhotoResearch PR670 spectroradiometer, along with a Keithley 2400 Source Meter.

Acknowledgements

This work was financially supported by the National Natural Science Foundation of China (U23A20594, 22375066), the GuangDong Basic and Applied Basic Research Foundation (2023B1515040003, 2022A1515010315, 2021A1515110826) and the Science and Technology Program of Guangzhou, China (202201010439).

Author contributions

Z.Z. conceived the study. L.X. synthesized and characterized the materials, measured the photophysical property. L.X. and K.Z. analysis the experimental data. N.Q., J.Z. and H.L. fabricated and characterized the OLEDs. X.P. and L.X. performed theoretical simulation. L.X. and Z.Z. wrote and revised the manuscript. Z.Z. and B.Z.T. supervised the project. All authors discussed the results and commented on the manuscript. / All authors have given approval to the final version of the manuscript.

Competing interests

The authors declare no competing interests.

Additional information

Supplementary information is available for this paper.

https://doi.org/10.26434/chemrxiv-2024-qw671 **ORCID:** https://orcid.org/0000-0002-0618-6024 Content not peer-reviewed by ChemRxiv. **License:** CC BY 4.0